Effects of the Grazing Incidence Geometry on X-Ray Photon Correlation Spectroscopy Measurements

*Christopher R. Greve[a], Meike Kuhn[a], Fabian Eller[a], Michael A. Buchhorn[a], Alexander Hexemer[b], Guillaume Freychet[c,d], Lutz Wiegart[c] and Eva M. Herzig[a]**

[a]Herzig Group – Structure Formation and Dynamics, University of Bayreuth, Universitätsstr. 30, Bayreuth, Bavaria, 95447, Germany

[b]Advanced Light Source, Lawrence Berkeley National Lab, 1 Cyclotron Rd, Berkeley, CA, 94720, USA

[c]National Synchrotron Light Source II, Brookhaven National Laboratory, 98 Rochester St, Upton, New York, 11973, USA

[d]Université Grenoble Alpes, CEA, Leti, 17 Av. des Martyrs, F-38000 Grenoble, France

ABSTRACT X-Ray Photon Correlation Spectroscopy (XPCS) is a versatile tool to measure dynamics on the nanometer to micrometer scale in bulk samples. XPCS has also been applied in grazing incidence (GI) geometry to examine dynamics of surface layers. However, considering GI scattering experiments more universally, the GI geometry leads to a superposition of signals due to reflection and refraction effects, also known from the Distorted Wave Born Approximation (DWBA). In this paper the impact of these reflection and refraction effects on the correlation analysis is determined experimentally by measuring grazing incidence transmission XPCS (GT-XPCS) and grazing incidence XPCS (GI-XPCS) simultaneously for a thin film sample, showing non-equilibrium dynamics. Results of the GI and GT geometry comparison are combined within the framework of the standardly applied, simplified DWBA. These calculations allow identifying the main contributions of the detected signal from the leading scattering terms along the out-of plane direction q_z, which dominate the measured intensity pattern on the detector. In combination with the calculation of the non-linear effect of refraction in GTSAXS and GISAXS, it is possible to identify experimental conditions that can be chosen to run experiments and data analysis as close as possible to transmission XPCS and to explain which limitations for data interpretations are observed. Consequently, the beam exposure can be significantly reduced by using GI geometry only. Calculations of experimental settings prior to experiments are detailed to determine suitable q_z regions for a variety of material systems measured in bulk-sensitive GI-XPCS experiments allowing us to determine the scaling behavior of typical decay times as a function of q that is comparable to the scaling behaviour obtained in distortion free GT-XPCS or transmission XPCS experiments.

INTRODUCTION X-ray Photon Correlation Spectroscopy (XPCS) is a coherent scattering technique to measure the dynamics of structures in bulk materials. Measured in transmission geometry it is therefore widely used for determining equilibrium and non-equilibrium dynamics in colloidal systems such as gels [1] and suspensions [2], as well as polymeric glass formers [3]. To apply dynamical analysis to thin films, scattering measurements are carried out in grazing incidence (GI) geometry, allowing the probing of three-dimensional dynamical morphologies in thin films [4] as well as measurements on liquids [5]. In GI geometry the glancing incident angle enhances the scattered intensity due to the extended beam projection on the thin film sample [6]. There are several publications, where GI-XPCS was used to measure dynamics of thin soft matter systems on surfaces and at interfaces or growth mechanisms on various surfaces [7–11]. In these examples conditions were chosen such that the investigation concentrated on the examination of surface scattering only, i.e. via the generation of a dominantly reflected signal. [7,10–12] However, many questions in interface science in the context of thin films arise due to mechanisms originating within the bulk of the thin film that are additionally influenced by the interfaces towards the substrate and their surrounding. To examine the dynamics arising from the bulk of the film, several different scattering terms need to be taken into account and the interpretation of such GI data in the context of XPCS is not straight forward. Zhang et al. [9] showed that effects known from grazing incidence small angle x-ray scattering (GISAXS) need to be accounted for in a GI-XPCS analysis focused on bulk properties. The first effect is related to reflection, generating an additional scattering channel, shifted proportionally to the incident angle [13]. The second GI-effect is related to refraction, shifting the projection of reciprocal space on the detector. Before interpreting GI-XPCS data, it is therefore necessary to consider the effect of these different contributions arising from the (1) reflection and (2) refraction effect occurring in thin films. While static GISAXS data can be well approximated taking the Distorted Wave Born Approximation (DWBA) and refraction into account, this is not straight forward for time-resolved intensity fluctuations and extracted signatures thereof since different contributions with different dynamics mix within a single pixel. When encountering contribution mixing in GI-XPCS, Zhang et al. [9] showed that for certain reciprocal q_z regions the trend in contribution mixing is reversed along q_z. The authors show that after carrying out several measurements they can identify a region of interest in the scattering pattern where an analysis analogously to transmission XPCS can be carried out along q_r. While the overall shape of the intrinsic correlation curve is still altered due to the superposition of refraction and reflection contributions, at least the changes in scaling behavior of correlation times with q_r can be attributed appropriately to changes in temperature. In addition, interference of homo- and heterodyne scattering can occur [12,14], which further complicates the evaluation of extracted correlation curves.

To systematically examine the effect of the grazing incidence geometry on the intensity fluctuations and further on the extracted dynamics in bulk sensitive GI-XPCS, we first examine reflection and refraction effects theoretically. For the evaluation of reflection effects, we calculate the different contributing scattering channels based on Fresnel coefficients[15] and examine their individual relevance at different exiting scattering angles. In the next step we quantify the refraction effects[13] for different incident and exit angles. We use this theoretically obtained information to identify measurement conditions where we expect q_z regions dominated solely by the transmission channel. To demonstrate the dominance of the transmission channel we experimentally compare a grazing incidence transmission (GT)-XPCS measurement (known dominance of transmission), with a GI-XPCS measurement (assumed dominance of transmission). For this we measured GT- XPCS and GI-XPCS simultaneously using a detector examining a single sample that exhibits non-equilibrium dynamics induced by beam damage and used standard XPCS analysis steps to extract q-dependent 'aged' One-time correlation functions (aged-1TCF) (see SI section S1). In GT-XPCS the incident beam is directed to the downstream edge of the sample under a glancing angle above the critical angle[16,17]. The sample scattering then exits through the sample edge below the horizon. In this GT geometry, scattering contributions due to reflection events are avoided and refraction events are reduced[16]. Still, the GI geometry is more commonly used because it can be applied to a larger variety of thin film samples. This is due to experimental reasons. GT experiments require extremely precise alignment and certain sample quality conditions are not straight forward to fulfill rendering the GI geometry more robust and versatile. In the experiments we examine a thin film sample of Methylammonium lead iodide ($MAPbI_3$) that is exposed to a high energy beam, by which beam damage-driven dynamics are induced. For this disperse sample we calculate 1) Fresnel coefficients which determine the scattering contributions in the GI geometry[18] (calculations see SI section S2 & S3) and 2) the effect of non-linear refraction on the intensities related to intrinsic Q projected on the detector q [13,16] (calculations see SI section S4).

Both calculations are necessary to show the origin of the measured scattering contributions when comparing the distortion reduced GT signal (dominated by scattering captured within the Born Approximation (BA) [19]) and the distorted GI-XPCS signal (superposition of scattering contribution within the DWBA [20]). As known for both geometries the generated scattering signal directly depends on the incident and exit angles [16,18], therefore we calculate and analyze several parameters, for incident and exit angles experimentally accessible with a single large 2D detector for simultaneous GT and GI-XPCS measurements.

THEORETICAL BASIS

Both grazing incidence geometries, GT and GI, introduce reflections at the substrate surface, which results in multiple reflection and scattering combinations (MRSCs) that need to be considered when calculating the intensity at the detector. To mathematically describe the static intensity distribution across the detector, all possible sequences of transmission, reflection and scattering events need to be considered. One approximation to solve the problem is known as the Distorted-wave Born Approximation (DWBA)[20]. For the disperse system examined within the study the DWBA can be employed within its simplified form (see SI Section S2 for full derivation) describing the intensity on the detector $I_d(q_z)$:

$$I_d(q_z) = \left|T_i T_f\right|^2 |F(+Q_{z1})|^2 + \left|R_i T_f\right|^2 |F(+Q_{z2})|^2 + \left|T_i R_f\right|^2 |F(-Q_{z2})|^2 + \left|R_i R_f\right|^2 |F(-Q_{z1})|^2 (1)$$

Herein $Q_{z1} = k(\sin\alpha_i + \sin\alpha_f)$ and $Q_{z2} = k(\sin\alpha_i - \sin\alpha_f)$ with $k = 2\pi/\lambda$ and λ the wavelength of the incident x-ray beam and α_i and α_f being the scattering angles introduced in Fig. S5. Further, $T_{i/f}$ is the Fresnel coefficient of transmissivity for incident angle α_i/exit angle α_f and $R_{i/f}$ the respective Fresnel coefficients of reflectivity. The term *F(Q)* is the scattering strength contribution from the form factor. For disperse systems, *F(Q)* decays steadily without oscillations. The four terms in Eq. (1) can be split into two scattering channels, the transmitted scattering channel (Tc) (1), associated with the classical reciprocal space vector Q_{z1}, and the reflection scattering channel (Rc) (2), associated with the shifted reciprocal space vector Q_{z2}. In GT geometry Equation (1) is reduced and only the terms dependent on $\left|T_i T_f\right|^2$ and $\left|R_i T_f\right|^2$ remain [16], because terms dependent on $\left|T_i R_f\right|^2$and $\left|R_i R_f\right|^2$ result on scattering with an exit angle above the sample horizon only observable in GI geometry.

To check for dominant terms of scattering along the detector we modelled our sample with a two-slab system of $MAPbI_3$ at 9.65 keV x-rays (800 nm thickness, 10 nm roughness, critical angle θ_c = 0.163°) on a silicon substrate (critical angle θ_{si} = 0.186°). The calculation of Fresnel reflectivities R_i and R_f and transmissivities T_i and T_f is based on the standard method given by Renaud et al. [15]. Further information can be found in the SI (Section S3).

Comparing the relative contribution of each DWBA term, i.e. by examining the prefactor fraction, we can learn which terms dominate the scattering pattern for a particular q_z and θ_i. The sum of prefactors is normalized and plotted versus q_z. This presentation of the data allows identifying dominant terms dependent on the incident angle θ_i. In Fig. 1a, we show the results for two different incident angles θ_i. The GTSAXS region is seen around $q_z = 0$ below the empty gap. The empty gap arises from inaccessible scattering regions resulting from reflection of scattering below the substrates critical angle (lower q_z limit) and the sample horizon (higher q_z limit). For GTSAXS only the discussed two DWBA terms remain, with the prefactor $|T_i T_f|^2$ becoming more dominant with increasing incident angle. This is the prefactor related to direct scattering described within the Born Approximation (BA), which is used to describe scattering in a transmission geometry. Consequently, with higher incident angles (here: $\theta_i = 0.30°$) the intensity on the detector approaches the same origin as in transmission geometry, indicating that GT-XPCS signal will have the same origin as in transmission XPCS for an increased incident angle. This does not hold true for small incident angles, like $\theta_i = 0.22°$, where the reflection term related to $|R_i T_f|^2$ still contributes (see Figure 1a). The GISAXS region is seen above the empty gap and shows that above the sample horizon and below the Yoneda-region [21] scattering is dominated by DWBA prefactors $|T_i T_f|^2$and $|T_i R_f|^2$. Within the Yoneda region all terms are present, but above this region the contribution of the term $|T_i R_f|^2$ is reduced with increasing q_z. Fig 1a shows that for the material system tested here, for q_z values of 0.045 Å^{-1} for $\theta_i = 0.22°$ and 0.055 Å^{-1} for $\theta_i = 0.30°$ the contributions related to $|R_i R_f|^2$and $|T_i R_f|^2$ vanish. The weights of the prefactors return their incident angle dependent GTSAXS equivalents, with the BA term (with prefactor $|T_i T_f|^2$) becoming dominant for larger incident angles like $\theta_i = 0.30°$. This meets the expectation by Lazzari et al. [18] that for high incident and exit angles the BA prefactor becomes dominant in GI geometry.

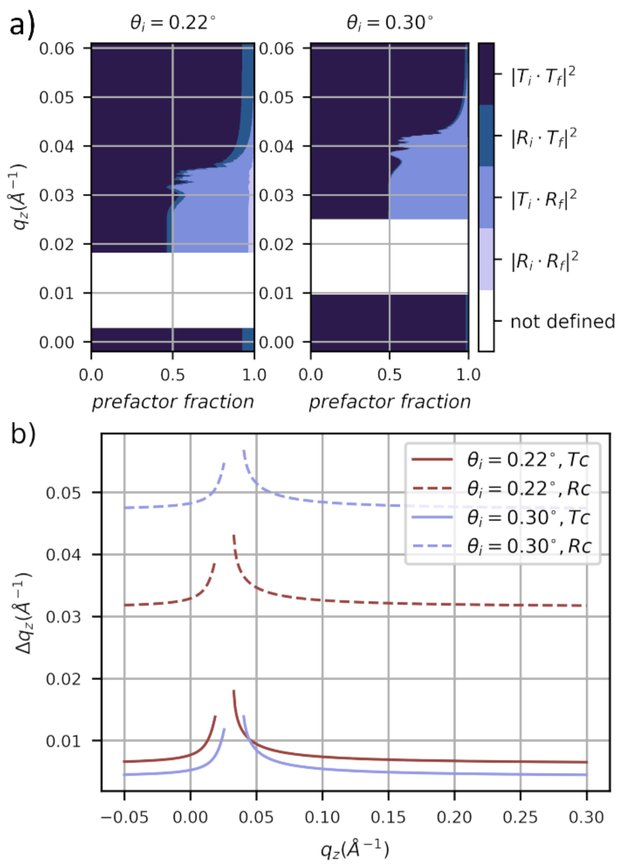

Figure 1. a) Plot of the normalized prefactor fraction of Fresnel coefficients used for intensity calculations in the simplified DWBA for the incident angles $\theta_i = 0.22°$ ($\theta_i/\theta_c = 1.35$) and 0.30° ($\theta_i/\theta_c = 1.84$) versus q_z. The reflectivities and transmissivities are calculated for a two-slab system of 800 nm thick $MAPbI_3$ placed on a silicon substrate with varying exit angles θ_f. The q-conversion is done via $q_z = 2\pi/\lambda[\sin(\theta_i) + \sin(\theta_f)]$. b) The difference between detector q_z and intrinsic Q_z originates from the refraction effects ($\Delta q_z = q_z - Q_z$) vs detector q_z for incident angles of $\theta_i = 0.22°$ (brown lines) and 0.30° (blue lines). Scattering from the Transmission channel (Tc, solid) and Reflection channel (Rc, dashed) are calculated separately.

As introduced earlier, another important influence on the detected intensity pattern is the effect of refraction at interfaces between different materials. When the beam enters the thin film from vacuum/ambient atmosphere typically a small refractive index change occurs ($\Delta n < 10^{-6}$), independent of measurement geometry. But the combination of the differences in refractive index and the small incident angle in GI and GT geometry leads to relevant beam refraction at the interface. Therefore, in contrast to transmission SAXS the scattering pattern obtained by GTSAXS and GISAXS is distorted when projected onto the detector. As depicted in Fig. S5 refraction will occur at interfaces and the incident beam and scattered x-rays will be shifted, altering angles within the sample [22,23]. Due to refraction altering detected angles it is necessary to distinguish between the intrinsic thin film reciprocal space Q within the thin film and the measured detector reciprocal space q. The intrinsic reciprocal space Q is defined as:

$$Q = 2k\sin(\alpha_s), \qquad (2)$$

where k and λ follow the earlier definition and α_s is the scattering angle within the thin sample (as introduced in Fig. S5). In contrast the detector reciprocal space is defined as $q = 2k\sin(\theta_s)$, with θ_s being the scattering angle outside the thin sample (see Fig. S5). As shown by Lu *et al.* [16] the difference between intrinsic Q and detector q is highly non-linear near the critical angle θ_c of the impinged thin film. Importantly, the refraction affects only the z-direction and (for the small angles used here) will not alter the shift in the scattering signal on the detector along the horizontal q_r-component.

To illustrate the non-linear contribution of refraction [13,16] to the projection of scattering onto the detector, we calculate the difference between intrinsic Q and detector q as $\Delta q_z = q_z - Q_z$. Two different cases need to be distinguished. The transmission channel (Tc) addresses the scattering contributions containing no or double reflections (valid for $\left|T_i T_f\right|^2 |F(+Q_{z1})|^2$ and $\left|R_i R_f\right|^2 |F(-Q_{z1})|^2$). In the reflection channel (Rc) (valid for $\left|R_i T_f\right|^2 |F(+Q_{z2})|^2$and $\left|T_i R_f\right|^2 |F(-Q_{z2})|^2$) we take into account the known shift of the scattering in Rc in relation to Tc, which is proportional to $2\theta_i$ [24]. The derivation of Q_z for Rc and Tc depending on the scattering angles outside the sample is shown in the SI (Section S4).

A plot of Δq_z vs q_z is given in Fig. 1b, showing the non-linear influence of refraction on the projection of intrinsic Q_z onto detector q_z for two incident angles θ_i. The vertical shift in the Δq_z curve between the Tc and Rc increases with higher incident angle since the difference between intrinsic Q_z and detector q_z originates from the finite incident angle combined with an odd number of reflection processes. The non-defined q_z region results from the same reasons given when discussing Fig. 1a.

Combining the information from DWBA prefactors (reflection effects, Fig. 1a) and from nonlinear reciprocal space vector projection (refraction effects, Fig. 1b) allows us to conclude the following points for a comparison of transmission XPCS and XPCS results in grazing incidence geometries.

Firstly: Fig. 1a shows that for high incident angles (θ_i = 0.30°) the scattering in the GT region and high q_z GI region is dominated by the BA term. While for lower incident angles the scattering contributions from both transmission and reflection channels are mixed on the detector, consequently influencing the shapes of extracted correlation functions. The dominance of BA related scattering does not imply that e.g. correlation times are identical, because the absolute q-value given by $q = \sqrt{q_r^2 + q_z^2}$ generally differs in GTSAXS where $q_z = 0$ and GISAXS where $q_z > 0$. However, we propose for a heterogeneous system with no dominating characteristic length scales, no changes to the nature of the underlying dynamics over the combined q-ranges are expected. As a result, the scaling behavior of τ with q will be comparable for GT- and GI-XPCS.

Secondly: Fig 1b shows that refraction alters the projection of intrinsic Q onto the detector. For higher incident angles the discrepancy between intrinsic Q and detector q is globally reduced for Tc but will still lead to the examination of a different intrinsic Q in transmission XPCS than in GT- and GI-XPCS. This leads to associated changes in the correlation functions when compared to the same detector q in a transmission XPCS experiment. Calculating the influence of refraction allows us to conclude, which detector q-values in transmission XPCS and GT-and GI-XPCS are comparable. For accessible q_z in GI up to ~ 0.06 Å^{-1} (see Section S5 for discussion) the difference in Δq_z is not yet minimized or as low as in GT-XPCS measured at q_z = 0.0 Å^{-1}. For q_z below ~ 0.06 Å^{-1} and when Tc and Rc channels contribute to the detected signal, different intrinsic Q_z values contribute to the recorded intensity within an analyzed Region of Interest (ROI) in GI-XPCS, influencing the aged One-time correlation function (aged-1TCF) shape in comparison to GT-XPCS and resulting in expected differences in parameters like stretching exponents and correlation times. This contribution mixing can only be suppressed if only one of Tc or Rc is contributing.

Additionally, other experimental settings like beam size (scattering from front and end of the beam footprint on sample) and the size of the analyzed ROI also contribute to a certain degree of mixed intensity contributions. Therefore, we calculated how the finite sample size, the detector pixel size and the size of our evaluated ROIs from Fig. S2 lead to mixed q_z on the detector (details see section S6). We can conclude that the influence of mixing of different q_z within a single pixel, as well as the influence of changes of the sample detector distance (SDD) by the extended footprint on the sample is negligible and up to three orders of magnitude smaller than the effect introduced by Δq_z caused by refraction effects shown in Fig. 1b. Further shows Fig. S8 that the size of the ROIs along q_z (see Fig. S2 for ROIs) have a bigger impact on the analysis than the SDD and single pixel size.

Still the Δq_z shift caused by finite ROI size along q_z (here: Δq_z = 0.003 $Å^{-1}$) is several times smaller than the shift Δq_z seen in Fig. 1b for the q_z-discrepancies induced in Tc and more than one order of magnitude smaller in comparison to those induced in the Rc.

MATERIALS AND METHODS

Materials. Materials for thin films of a metal halide perovskite solar cell were used as received. Methylammonium iodide (MAI) was bought from Greatcell Solar and Lead(II) iodide (PbI_2, 99,99% trace metal basis) was obtained from Tokyo Chemical Industry. Solvents used for precursor dissolution were Tetrahydrofuran (THF), stabilised, purchased from BerndKraft and Methylamine, 33% in absolute Ethanol acquired from Aldrich. Solvents used to clean the silicon substrates (SiegertWafer, 1000 ± 20 µm, PIB, <100> ± 0.5°) were deionized (DI) H_2O, H_2O_2 (30%, stabilised, VWR) and H_2SO_4 (95% - 97%, for analysis, Merck).

$MAPbI_3$ thin film preparation. Thin films of Methylammonium lead iodide ($MAPbI_3$) were produced on silicon substrates by slot-die coating in a one-step process. The cleaved silicon substrates were first cleaned 15 min in an acid bath (54 ml of DI water, 84 ml of H2O2 and 198 ml of H2SO4), heated to 80°C. After rinsing with DI water and drying with pressurized nitrogen, the Si substrates were functionalized with O2 plasma (Plasma Technology GmbH, 0.1 bar, 5min). For thin film preparation metal halide precursors (MAI and PbI2) were dissolved in a solution of Methylamine in ethanol and THF (1:1 volume ratio) to get a final precursor concentration of 0.5 mol. The prepared $MAPbI_3$ precursor solution was used to slot-die coat thin films with a custom-built setup under ambient atmosphere [25] on the prepared Si substrates. The slot-die parameters were the following: 200 µm gap distance between slot-die head and substrate, 30 mm/s coating speed, 30 mm/s^2 coating acceleration and 50°C substrate bed temperature. After a resting time of approximate 30 s after the finished slot-die coating process, the thin films were transferred to a heat plate and annealed for 10 min at 140°C. Finished films were around 800 nm thick (as measured by Dektak 150, Veeco) and cleaved to 2 cm x 1 cm size to produce clean edges for GTSAXS experiments. The cleaved films were stored until use in a nitrogen filled glovebox at RT.

XPCS Measurements. Simultaneous GT-GI-XPCS experiments were conducted at the 11-ID Coherent Hard X-Ray (CHX) beamline at the National Synchrotron Light Source II (NSLS II) at the Brookhaven National Lab. The photon energy was fixed to 9.65 keV (wavelength λ = 1.285 Å) with a beam size of 10 x 10 μm^2 defined by slits. Intensity patterns were captured using an

Eiger X 4M detector with a sample-detector-distance of 13 m and a pixel size of 75 μm. To induce dynamics in a static $MAPbI_3$ sample 120 s of unattenuated beam were administered to the sample under grazing incidence with incident angles of $\theta_i = 0.22°$ and 0.30° ($\theta_i > \theta_c$, bulk-sensitive) for which 600 detector images with an exposure time of 0.2 s and a frame rate of 5 Hz were recorded. The resulting footprints were 2.6 mm and 1.9 mm, but halved by the requirement for edge-near measurements in GT geometry. With an unattenuated flux of $5x10^{11}$ ph/s for the beam the respective photon flux on the sample were 1.9 x 10^7 ph/s/ μm^2 and 2.6 x 10^7 ph/s/ μm^2. The administered 120 s of unattenuated beam is 240 times higher than the measured threshold for beam damage of 0.5 s (~ 1.0 x 10^7 ph/μm^2) at an incident angle of 0.30° and induced degradation within the thin film. The chosen flux was i) necessary to gather sufficient photon statistics within the GT-region of the detector and ii) allowed to induce beam-damage-driven dynamics in the sample. To circumvent build-up of x-ray dose in measurement spots the sample was translated by a minimum of two times the beam size between measurements for subsequent measurements. Subsequent measurements of $\theta_i = 0.22°$ and 0.30° were taken on the same $MAPbI_3$ sample. The calculation of autocorrelation functions (for details on the calculations see SI section S1) was performed using the computing infrastructure and Python code provided by the CHX beamline staff (see NSLS II on Github, [26])

RESULTS AND DISCUSSION

Simultaneous GT-GI-XPCS measurements. To test the theoretical considerations shown in the section Theoretical Basis on the origin of detected intensities and their impact on measured dynamics in GT- and GI-XPCS we conducted simultaneous GI-GT-XPCS measurements on a $MAPbI_3$ thin film (see Materials and Methods). The film consists of grains, ranging from several tens of nm up to several hundred nm leading to a scattering signal without Kiessig fringes and a q^{-n} decay. The experimental set-up geometry and incident angles were chosen such that the GT- and GI-signal can be recorded simultaneously on the same 2D detector, while the x-ray beam penetrates inside the film allowing for bulk-sensitive GI-XPCS measurements. This ensures measuring identical dynamics of beam damage-driven degradation in GI and GT geometry simultaneously, but limits the observable q_z range to a $q_{z,max}$ of 0.06 Å^{-1} (see Fig. S2 for ROIs).

Fig. 2a shows the correlation time τ_0 against q_z taken for a deterioration time $\bar{t}$ of [50 ± 2] s. The dependence of τ_0 on q_z above the GT region is related to the fact that different length scales are probed, resulting in different correlation times present. For intermediate regions of q_z (q_z < respective Yoneda) flat regions arise (dotted lines in black). Zhang et al. [9] attribute these flat regions in q_z to mixing of scattering signals from the Tc and Rc originating from different Q_z. The overlapping contributions of Tc and Rc scattering signal vary in between the Yoneda region and the specular beam position and roughly cancel due to opposing intrinsic Q_z trends, resulting in flat q_z regions. Within the flat regions most of the q-scaling of τ_0 is governed by the scaling of τ_0 vs q_r and hence can be used to analyze the present dynamics in the sample according to Zhang et al. [9]. Fig 2b shows the Kohlrausch-Williams-Watts (KWW) exponent γ against q_z from the aged-1TCF fits. In the GT region at $q_z = 0.0$ Å^{-1} γ values around 1.5 to 1.7 are observed, while an increase with increasing q_z from 1.5 up to 2.0 is obtained in the GI region for $\theta_i = 0.30°$ and an increase from 1.2 up to 1.7 for $\theta_i = 0.22°$. Due to our measurement approach of simultaneous GI-GT-XPCS measurements, the probed underlying physical behaviour is expected to be identical in GI and GT geometry. Nevertheless, we observe significant differences between $\gamma_{GT} = 1.7$ ($\theta_i = 0.22°$, $q_z = 0.0$ Å^{-1}) in GT and $\gamma_{GI} = 1.2$ ($\theta_i = 0.22°$, $q_z = 0.02$ Å^{-1}) in GI within the same measurement. It is known that γ, which is a descriptor of the sample dynamics, can vary with q. But the dependence of γ to q does not explain the sharp jump between γ_{GT} and γ_{GI}. Without characteristic length scales within the sample γ should vary slowly with q [1]. Sharp jumps would only be expected when characteristic length scales are crossed e.g. during structural rearrangements[1,27], but in a heterogeneous system of multi-sized crystalline grains no such length scale is dominant. Consequently, the sharp change in γ between GI and GT regions of q_z is attributed to the influence of refraction and MRSCs, altering the shape of analysed aged-1TCFs. However, the GI data for $\theta_i = 0.22°$ for $q_z > 0.05$ Å^{-1} reach the value of γ_{GT}. This is in line with the expectations based on the prefactor fractions from Fig. 1a, which show that for high q_z values, the prefactor fractions from the GT range are reached. Although for an incident angle of 0.22° these are not dominated by Tc alone as for 0.30° (explaining the difference between γ_{GT} of $\theta_i = 0.22°$ and $\theta_i = 0.30°$), comparable prefactor fractions are nevertheless achieved. In contrast, comparable γ are not achieved for high q_z for $\theta_i = 0.30°$. We expect that comparable values could be reached for $q_z > 0.06$ Å^{-1}, since possibly the influence of the difference between intrinsic Q_z and detector q_z is not yet linear enough (see Fig. 1b).

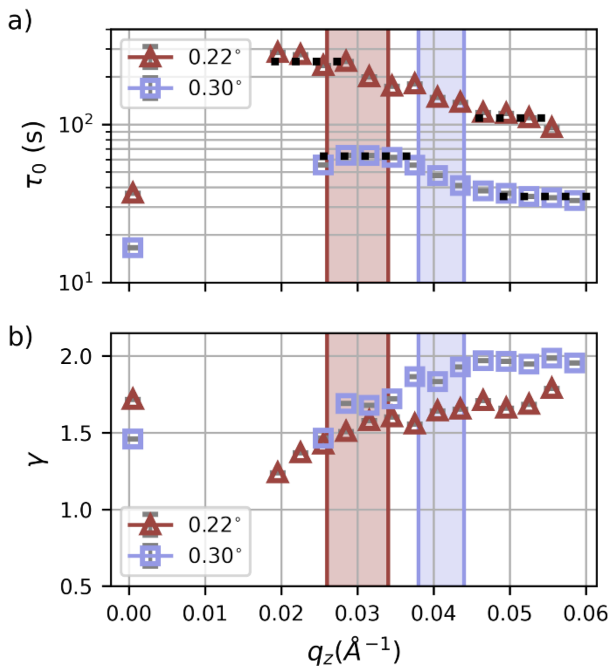

Figure 2. a) Graph of correlation times τ_0 against q_z and b) KWW exponent γ against q_z for a slot-die coated $MAPbI_3$ thin film in simultaneous GI/GT geometry for various incident angles around q_r = 0.0035 $Å^{-1}$. Error bars are given in grey and are smaller than the marker size. The incident angle-dependent Yoneda regions are marked in the respective colour. Flat regions identified after Zhang et al. [9] are marked as dotted lines in black. Identified flat regions were adapted with permission from Ref. 9, Copyright 2019 American Physical Society.

Scaling Analysis of extracted 1TCF parameters. To further investigate the differences in dynamics in GI and GT-XPCS the proposed approach by Zhang et al. [9] is used to investigate the scaling of τ_0 vs q_r within flat regions of τ_0 vs q_z. The ROIs along q_r are shown in Fig. S2 a) and c) and their respective aged-1TCFs in Fig. S3 and S4. The results on the scaling of τ_0 vs q_r are shown in Fig. 3 for 3 different q_z regions. The scaling behaviour of τ_0 vs q_r varies depending on the incident angle and measurement geometry. The observed process is a surface activated ionization and destruction process of the $MAPbI_3$ thin film. Therefore, bulk sensitive conditions ($q_z \sim 0$ or high θ_i and high q_z) show a weaker dependence of q_r. In contrast, the more surface sensitive condition of $\theta_i = 0.22°$ at intermediate q_z (below the Yoneda-region) examines the destruction mechanism on the sample surface leading to a stronger scaling with q_r. As argued within the section on theoretical considerations in GI geometries the scaling behavior for τ_0 vs q for an incident angle of 0.30° should show comparable scaling dynamics in the GTSAXS region and the GISAXS region at $q_z > 0.055$ Å^{-1} because the scattering signal in these detector regions stem from only one DWBA scattering contribution ($\left|T_i T_f\right|^2 \ |F_{+1}|^2$). To test this expectation, we project the scaling of τ_0 vs q_r in GT (Fig. 3a, dashed line) to q *via* $q = \sqrt{q_r^2 + q_z^2}$ and compare it to τ_0 from the GI data points for both incident angles in Fig. 2a projected to q. The result of the projection to q is shown in Fig. 4. To visualize the scaling in GT in comparison to GI the slope of the GT data points was shifted as a guide-to-the-eye (dashed-dotted line). The graph shows that the scaling behavior of τ_0 in GT converges with the high q_z-data in GI for $\theta_i = 0.30°$, in contrast to $\theta_i = 0.22°$ for which the data points are not converging on the guide-to-the-eye. The presented plot therefore indicates that the higher the angle of incidence is, the lower the q for which this scaling applies, in accordance with the dominance of the BA term. Therefore, we attribute the deviation of the τ_0-scaling behavior for lower q in Fig. 4 to the additional DWBA terms resulting in mixing of Tc and Rc scattering and the respective non-linear refraction changes occurring in that q-range.

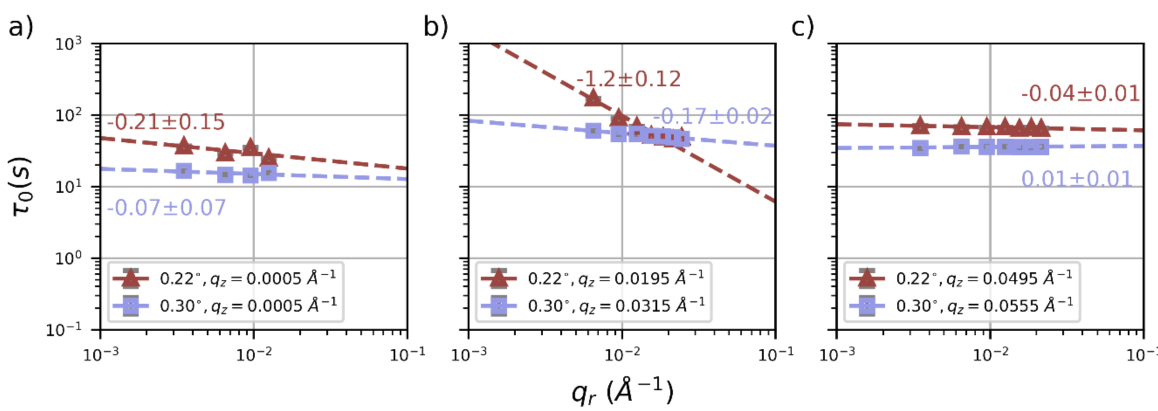

Figure 3. The graphs show fit results from the aged-1TCF and the resulting comparison of the scaling behavior of the average value of the correlation time τ_0 versus q_r between GT data (extracted near $q_z = 0$) in a), as well as surface (b) and bulk (c) sensitive q_z regions for GI data (for comparison reasons located below and above the respective Yoneda regions), where according to Zhang et al. dynamics are solely represented by their q_r scaling. Error bars are given in grey and are smaller than the marker size. For an incident angle of 0.22° scattering stems in all subfigures from Rc and Tc scattering contributions. For an incident angle of 0.30° subfigures a) and c) are

dominated by scattering from Tc scattering, while contributions from Tc and Rc are present in b) (see Fig. 1a). Numbers above each dashed line mark the slopes of a linear fit in the log-log graph.

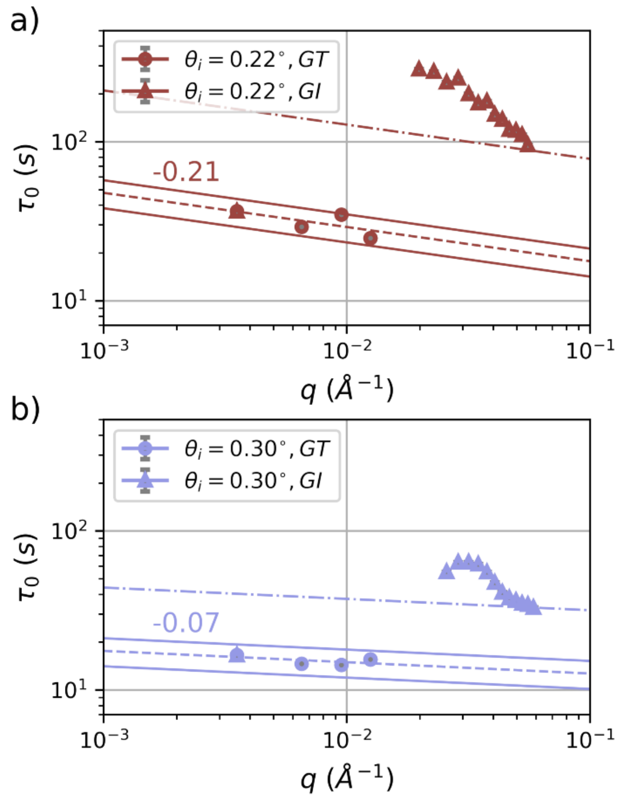

Figure 4. The graph shows fit results from aged-1TCFs and the relevant comparison of correlation times τ_0 vs q for extrapolated GT data (circles, taken from GT data points along q_r in Fig. 3) and GI data (triangles, taken from GI data points along q_z in Fig. 2) for 0.22° (a) and 0.30° (b). Error bars are given in grey and are smaller than the marker size. Numbers under dashed lines mark the slopes of a linear fit in the shown log-log graph for GT data. The correlation time τ_0 behaviour was extrapolated from GT data to high q-values via the scaling exponent (linear slope). The solid lines are variations to the extrapolated τ_0 by ± 20 % to take into account uncertainties, influencing the refraction within the thin film and altering nominal q_z for the GI data (after Zhang et al. [9]). The dashed-dotted lines are a guide-to-the-eye having the same slope as the dotted lines. Uncertainties were adapted with permission from Ref. 9, Copyright 2019 American Physical Society.

Identification of suitable q_z regions. We aim to use simultaneous GI-GT-XPCS measurements to demonstrate that several regions on the detector can be used to extract comparable dynamics to bulk sensitive transmission XPCS measurements, while other regions suffer from intensity variations due to MRSC and refraction effects. We propose that the data that is most comparable to transmission XPCS is in the GT region, when using high incident angles. For the GT region, we can show in Fig. 1b for an incident angle of 0.30° that an offset to correlation times τ_0 in comparison to transmission XPCS occurs, due to the refraction effect on the projection of intrinsic Q to detector q. But under consideration of the dominant scattering term $\left|T_i T_f\right|^2$ from Fig. 1a under the same incident angle we do not expect a systematic effect on the stretching exponent γ as a result from the combination of reflection and refraction effects. Further, we showed in Fig. 4 that the scaling behaviour of correlation times τ_0 vs q in the GT regions can be recovered in GI for large enough θ_i and high q_z regions which are dominated by the BA term (see Fig. 1a).

Care must be taken if the proposed approach by Zhang et al.[9] is used to analyze the scaling of τ_0 vs q_r. According to their work, in between the direct beam and the specular beam position the intrinsic Q_z from Tc and Rc overlap within the detector q_z with competing trends. Based on theoretical considerations on $Q_{z,GI,Tc}$ and $Q_{z,GI,Rc}$ (section S4, equation 3a and 3b) we calculated the absolute $|Q_z|$ against detector q_z. The result is seen in Fig. S7. The plot indicates that while $Q_{z,GI,Tc}$ shows a continuous increase with q_z, $Q_{z,GI,Rc}$ is decreasing from the Yoneda position up to the specular beam position, while increasing above the specular beam position. While the general trend of countervailing q_z for Tc and Rc is supported by our calculations, these calculations also show that the region to extract meaningful XPCS signals is further restricted. In addition, it is also necessary to consider the respective prefactors of Tc and Rc to identify valid q_z ranges for which Tc and Rc prefactors are approximately equal such that q_z shows competing Q_z trends. Combining information from Fig. 1a and S7 leads to expecting flat regions within the Yoneda regions, which are not present in our data set. We therefore anticipate that the flat q_z regions are false-positives and related to the effect of distortions in GI geometry which strongly influences the XPCS analysis shown in Fig. 3b, especially for an incident angle of $\theta_i = 0.22°$. The plot shows a slope of -1.2 in the log-log-plot of τ_0 as a function of q_r. However, the GT data at $\theta_i = 0.30°$, which are most close to a transmission XPCS measurement, show a much-reduced slope of -0.07 although we propose that the same dynamic process is probed. Such strong influence of reflection and refraction effects on the correlation times makes scaling analysis of correlation times in GI-XPCS data error-prone. To avoid errors in scaling analysis we suggest analyzing the results of Fresnel coefficients and refraction calculations in GI to identify which q_z-regions are suitable for XPCS analysis.

Influence of hetero- and homodyne detection schemes. Still, other effects might alter extracted aged-1TCF shapes. One such effect is the interplay of homo- and heterodyne detection schemes, which might occur in low q-regions. Based on Gutt et al.[12] we calculate the typical reciprocal length scale for interference to be $q \sim 5 \times 10^{-5}$ Å^{-1} (see S7 for further discussion). This value is more than 10 times smaller, than the lower q_r limit used within our GI experiments. Further, Sikharulidze et al.[28] showed that the contrast factor β jumps when changing detection schemes. Fig. S9 shows the contrast β vs q_r for GT and GI at various q_z. One can see that no jumps occur in β, further suggesting that solely a homodyne detection scheme is observed. Another point to consider is the projection of the coherence length in GI geometries. From Sikharulidze et al. [28] it is known that the projection of the coherence length onto the sample increases detected speckles per pixel, therefore reducing the measured contrast β. Due to the angle dependence of the projection this varies with the angle of incidence, but should not dominate the shape of measured aged-1TCF, despite reducing the contrast at low α_i.

Influence of coherence on wave vector spread and detector resolution. Gutt et al.[29] further included the influence of the coherence length on the wave vector spread $\delta q/q$ (see S8 for discussion), the detector resolution and pixel size and showed that both could induce a change of detection scheme from homo- to heterodyne in GI. They observed that these effects are pronounced at small detector openings or pixel sizes (< 30 µm) and for wave vector spreads >0.2. Due to the use of a 2D detector a plot of $\delta q/q$ with q_z is shown in Fig. S10. From the plot we see that we are below the identified $\delta q/q$ ratios of Gutt et al. for the q values used within this study. Along with the pixel size of 75 µm we conclude that these effects of partial coherence to aged-1TCF shapes can be excluded for our measurements with exceptions to altered contrast factors.

After consideration and exclusion of these well-known effects of partial coherence, resolution and detection scheme mixing we conclude that the effects seen within the manuscript are related to the geometrical effects mentioned in the theoretical section of the manuscript. We therefore can identify suitable regions of analysis with our chosen approach, relying on the calculation of refraction and MRSC effects. Both reflection and refraction effects alter the projection of intrinsic scattering on the 2D detector and depend on material properties. The refraction influence can be calculated with knowledge of the critical angle θ_c of the material, which can be measured in GISAXS experiments or calculated from the materials refractive index. Reasonable reflectivities and transmissivities are not as easy to estimate. But for experiments done on uniform films, meaning that the scattering contrast from structures within the film is significantly smaller than the scattering contrast between the thin film and the ambient atmosphere, reflectivities and transmissivities are well governed by the average film density and thickness, making an easy two-slab approach suitable[13]. This allows determining q_z regions most suitable for analysis for a large variety of material systems and strengthens the potential of bulk sensitive GI-XPCS for analysis of dynamic processes in thin films.

The presented approach is highly dependent on the sample (material, thickness) and measurement conditions (x-ray energy, incident angle). Therefore, we calculated further Fresnel coefficients for two materials (hybrid perovskite, polymer), two layer thicknesses (100s, 10s of nm) and x-ray energies (9.65 keV, 13.50 keV) (further details in section S9). The results are presented in Fig. 5 for 9.65 keV and Fig. S11 for 13.50 keV for ratios of incident angle to material critical angle of θ_i =1.1 θ_c, 1.5 θ_c and 2.0 θ_c. Fig. 5 shows that for $MAPbI_3$ an incident angle of 1.5 θ_c is sufficient that the BA scattering term is dominant around the specular beam position, while for P3HT an incident angle of 2.0 θ_c is necessary for the BA scattering term to become dominant. Furthermore, Fig. S11a shows that for $MAPbI_3$ at 13.50 keV already θ_i = 1.1 θ_c is mostly dominated by BA scattering around the specular beam position (sample thickness 800 nm). Due to the complexity of the relationship between material parameters and x-ray energy no simple rule-of-thumb can be established. While for the here chosen material systems and energies at θ_i = 2.0 θ_c the BA term is dominating around the specular beam position for all variables, scenarios exist (e.g., enhancement effects of interface layers or employed substrates) where this relationship could break down. Consequently, we recommend calculating the dominant scattering terms for specific experiments to identify the lowest angle at which the BA term dominates. This allows to maximize the overall scattering intensity that decays with increasing incident angle.

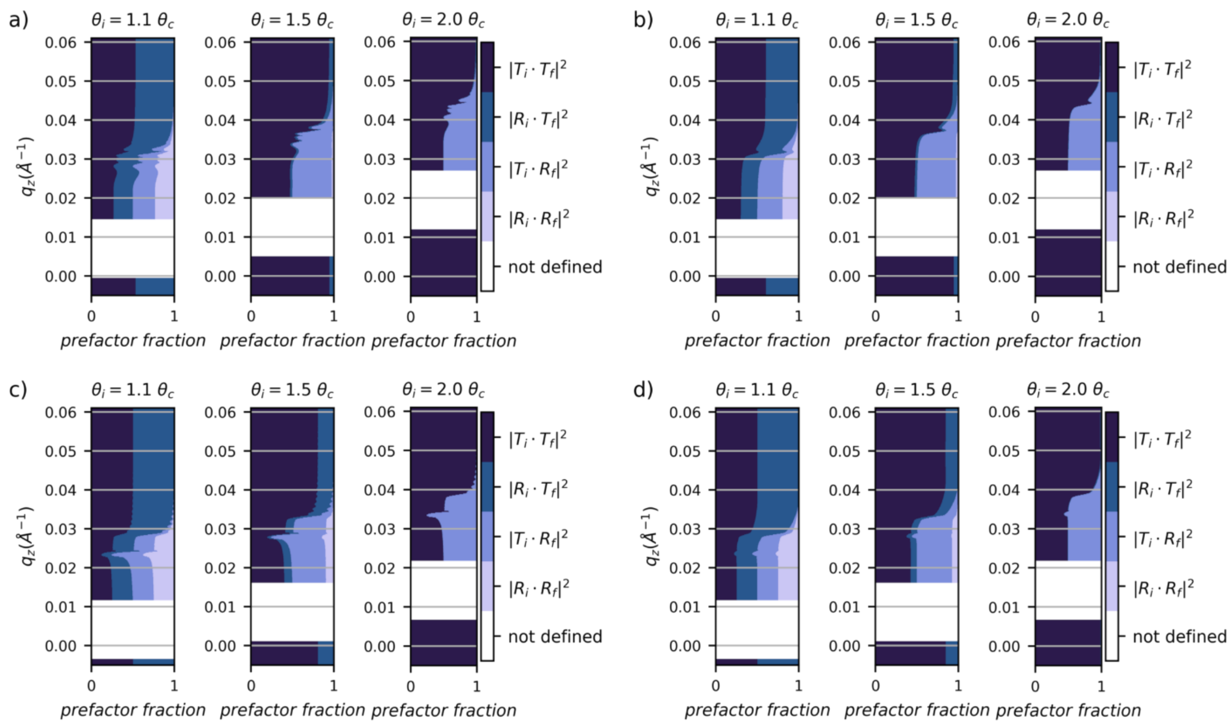

Figure 5. Material dependent Fresnel coefficient analysis used for intensity calculations in the simplified DWBA for incident angles θ_i = 1.1 θ_c, 1.5 θ_c and 2.0 θ_c versus q_z. The reflectivities and transmissivities are calculated for a two-slab system of a) 800 nm thick $MAPbI_3$ b) 20 nm thick $MAPbI_3$ c) 200 nm thick P3HT d) 20 nm thick P3HT placed on a silicon substrate with varying exit angles θ_f which is converted to q_z. Calculations are for an x-ray energy of 9.65 keV (λ = 1.285 Å).

CONCLUSIONS To move towards XPCS characterization of thin films beyond surface scattering dominated experiments, we have carried out calculations to reveal the dominant scattering terms as a function of incident angle within the simplified DWBA for bulk sensitive GT and GI scattering captured on a large 2D detector. In combination with the calculation of q space distortions by refraction in grazing incidence geometry we propose how reflection and refraction and resulting contribution mixing alter the observed dynamics from GI- and GT-XPCS in contrast to transmission XPCS. The expectations are probed by a study of simultaneously taken measurements of GT- and GI-XPCS, which allow us to identify regions in q_z and angle of incidence θ_i with comparable scattering origin in GI and GT geometry. This also holds true for incoherent GI and GT experiments. The presented approach enables the user to determine q_z regions suitable for GI-

XPCS experiments prior to experiments by systematically considering reflection and refraction contributions.

ASSOCIATED CONTENT

The following files are available free of charge.

XPCS data extraction; DWBA introduction; Fresnel reflectivity and transmissivity calculations; refraction influence to scattering origin in GI and GT; considerations on setup parameters and q-range for coherent scattering experiments; Q-mixing due to setup geometry and experimental ROIs; calculations on homo- and heterodyning; calculations on wave vector spread; generalization of incident angle approximation by Fresnel coefficients

AUTHOR INFORMATION

Corresponding Author

Eva M. Herzig - Herzig Group – Structure Formation and Dynamics, University Bayreuth, Universitätsstr. 30, Bayreuth, Bavaria, 95447, Germany; https://orcid.org/0000-0002-0151-5562; Email: eva.herzig@uni-bayreuth.de

Funding Sources

The research was funded through: Deutsche Forschungsgemeinschaft (DFG) trough TUM International Graduate School of Science and Engineering (IGSSE) (grant No. GSC 81); Bayerisches Staatsministerium für Wissenschaft und Kunst, Solar Technologies go Hybrid (SolTech); U.S. Department of Energy and BaCaTec.

Notes

The authors declare no competing financial interest.

ACKNOWLEDGEMENT

No conflict of interest must be declared. We thank Dinesh Kumar and the beamline team around Andrei Fluerasu for fruitful discussions and analysis tools. This research used beamline 11ID of the National Synchrotron Light Source II, which is a U.S. DOE Office of Science Facility at Brookhaven National Laboratory under Contract No. DE-SC0012704. EMH and CG thank the Bayerisches Staatsministerum für Wissenschaft und Kunst for funding in the framework of the „SolTechGoHybrid“ initiative and the Deutsche Forschungsgemeinschaft (DFG) for funding through TUM International Graduate School of Science and Engineering (IGSSE).

ABBREVIATIONS

aged-1TCF, aged One-time correlation function; DI, deionized; DWBA, Distorted Wave Born Approximation; GI, grazing-incidence; GT, grazing-incidence transmission; KWW, Kohlrausch-Williams-Watts; MAI, Methylammonium iodide; $MAPbI_3$, Methylammonium lead iodide; MRSC, multiple reflection and scattering combination; P3HT, Poly(3-hexylthiophene-2,5-diyl; PbI_2, Lead(II) iodide; Rc, reflection channel; SAXS, small angle x-ray scattering; Tc; transmission channel; XPCS, X-Ray Photon Correlation Spectroscopy.

REFERENCES

(1) Fluerasu, A.; Moussaïd, A.; Madsen, A.; Schofield, A. Slow Dynamics and Aging in Colloidal Gels Studied by X-Ray Photon Correlation Spectroscopy. *Phys. Rev. E* **2007**, *76*, 010401.

(2) Orsi, D.; Fluerasu, A.; Moussaïd, A.; Zontone, F.; Cristofolini, L.; Madsen, A. Dynamics in Dense Hard-Sphere Colloidal Suspensions. *Phys. Rev. E* **2012**, *85*, 011402.

(3) Conrad, H.; Lehmkühler, F.; Fischer, B.; Westermeier, F.; Schroer, M.; Chushkin, Y.; Gutt, C.; Sprung, M.; Grübel, G. Correlated Heterogeneous Dynamics in Glass-Forming Polymers. *Phys. Rev. E* **2015**, *91*, 042309.

(4) Hexemer, A.; Müller-Buschbaum, P. Advanced Grazing-Incidence Techniques for Modern Soft-Matter Materials Analysis. *IUCrJ* **2015**, *2*, 106–125.

(5) Proeller, S.; Liu, F.; Zhu, C.; Wang, C.; Russell, T. P.; Hexemer, A.; Mueller-Buschbaum, P.; Herzig, E. M. Following the Morphology Formation In Situ in Printed Active Layers for Organic Solar Cells. *Adv. Ene. Mater.* **2016**, *6*, 1501580.

(6) Smilgies, D.-M. Scherrer Grain-Size Analysis Adapted to Grazing-Incidence Scattering with Area Detectors. *J. Appl. Crystallogr.* **2009**, *42*, 1030–1034.

(7) Headrick, R. L.; Ulbrandt, J. G.; Myint, P.; Wan, J.; Li, Y.; Fluerasu, A.; Zhang, Y.; Wiegart, L.; Ludwig, J. K. F. Coherent X-Ray Measurement of Step-Flow Propagation during Growth on Polycrystalline Thin Film Surfaces. *Nat. Comm.* **2019**, *10*, 1–9.

(8) Jiang, N.; Endoh, M. K.; Koga, T. `Marker' Grazing-Incidence X-Ray Photon Correlation Spectroscopy: A New Tool to Peer into the Interfaces of Nanoconfined Polymer Thin Films. *Polym. J.* **2013**, *45*, 26–33.

(9) Zhang, Z.; Ding, J.; Ocko, B. M.; Fluerasu, A.; Wiegart, L.; Zhang, Y.; Kobrak, M.; Tian, Y.; Zhang, H.; Lhermitte, J.; Choi, C.-H.; Fisher, F. T.; Yager, K. G.; Black, C. T.

Nanoscale Viscosity of Confined Polyethylene Oxide. *Phys. Rev. E* **2019**, *100*, 1–8.

(10) Orsi, D.; Guzman, E.; Liggieri, L.; Ravera, F.; Ruta, B.; Chushkin, Y.; Rimoldi, T.; Cristofolini, L. 2D Dynamical Arrest Transition in a Mixed Nanoparticle-Phospholipid Layer Studied in Real and Momentum Spaces. *Sci. Rep.* **2015**, *5*, 17930.

(11) Amadei, F.; Thoma, J.; Czajor, J.; Kimmle, E.; Yamamoto, A.; Abuillan, W.; Konovalov, V. O.; Chushkin, Y.; Tanaka, M. Ion-Mediated Cross-Linking of Biopolymers Confined at Liquid/Liquid Interfaces Probed by In Situ High-Energy Grazing Incidence X-Ray Photon Correlation Spectroscopy. *J. Phys. Chem. B* **2020**, *124*, 8937–8942.

(12) Gutt, C.; Ghaderi, T.; Chamard, V.; Madsen, A.; Seydel, T.; Tolan, M.; Sprung, M.; Grubel, G.; Sinha, S. Observation of Heterodyne Mixing in Surface X-Ray Photon Correlation Spectroscopy Experiments. *Phys. Rev. Lett.* **2003**, *91*, 076104.

(13) Liu, J.; Yager, K. G. Unwarping GISAXS Data. *IUCrJ* **2018**, *5*, 737–752.

(14) Sinha, S.; Tolan, M.; Gibaud, A. Effects of Partial Coherence on the Scattering of X Rays by Matter. *Phys. Rev. B* **1998**, *57*, 2740–2758.

(15) Renaud, G.; Lazzari, R.; Leroy, F. Probing Surface and Interface Morphology with Grazing Incidence Small Angle X-Ray Scattering. *Surf. Sci. Rep.* **2009**, *64*, 255–380.

(16) Lu, X.; Yager, K. G.; Johnston, D.; Black, C. T.; Ocko, B. M. Grazing-Incidence Transmission X-Ray Scattering: Surface Scattering in the Born Approximation. *J. Appl. Crystallogr.* **2013**, *46*, 165–172.

(17) Vinogradov, N. A.; Harlow, G. S.; Carla, F.; Evertsson, J.; Rullik, L.; Linpe, W.; Felici, R.; Lundgren, E. Observation of Pore Growth and Self-Organization in Anodic Alumina by Time-Resolved X-Ray Scattering. *ACS Appl. Nano Mater.* **2018**, *1*, 1265–1271.

(18) Lazzari, R.; Leroy, F.; Renaud, G. Grazing-Incidence Small-Angle X-Ray Scattering from Dense Packing of Islands on Surfaces: Development of Distorted Wave Born Approximation and Correlation between Particle Sizes and Spacing. *Phys. Rev. B* **2007**, *76*, 125411.

(19) Van Hove, L. Correlations in Space and Time and Born Approximation Scattering in Systems of Interacting Particles. *Phys. Rev.* **1954**, *95*, 249–262.

(20) Sinha, S.; Sirota, E.; Garoff, S.; Stanley, H. X-Ray and Neutron-Scattering from Rough Surfaces. *Phys. Rev. B* **1988**, *38*, 2297–2311.

(21) Yoneda, Y. Anomalous Surface Reflection of X Rays. *Phys. Rev.* **1963**, *131*, 2010–2013.

(22) Breiby, D. W.; Bunk, O.; Andreasen, J. W.; Lemke, H. T.; Nielsen, M. M. Simulating X-Ray Diffraction of Textured Films. *J. Appl. Crystallogr.* **2008**, *41*, 262–271.

(23) Toney, M.; Brennan, S. Observation of the Effect of Refraction on X-Rays Diffracted in a Grazing-Incidence Asymmetric Bragg Geometry. *Phys. Rev. B* **1989**, *39*, 7963–7966.

(24) Resel, R.; Bainschab, M.; Pichler, A.; Dingemans, T.; Simbrunner, C.; Stangl, J.; Salzmann, I. Multiple Scattering in Grazing-Incidence X-Ray Diffraction: Impact on Lattice-Constant Determination in Thin Films. *J. Synchrotron Radiat.* **2016**, *23*, 729–734.

(25) Proeller, S.; Gonzalez, D. M.; Zhu, C.; Schaible, E.; Wang, C.; Mueller-Buschbaum, P.; Hexemer, A.; Herzig, E. M. Setup for Chemical Atmospheric Control during in Situ Grazing Incidence X-Ray Scattering of Printed Thin Films. *Rev. Sci. Instrum.* **2017**, *88,* 066101.

(26) Abeykoon, S. K.; Zhang, Y.; Dill, E. D.; Caswell, T. A.; Allan, D. B.; Akilic, A.; Wiegart, L.; Wilkins, S.; Heroux, A.; van Dam, K. K.; Sutton, M.; Fluerasu, A. Software Tools for X-Ray Photon Correlation and X-Ray Speckle Visibility Spectroscopy. In *2016 New York Scientific Data Summit (NYSDS)*; 2016; pp. 1–10.

(27) Widera, M.; Klemradt, U. Non-Equilibrium Processes in Martensitic Phase Transformations by. *MRS Online Proc. Libr.* **2015**, *1754*, 141–146.

(28) Sikharulidze, I.; Dolbnya, I.; Madsen, A.; de Jeu, W. X-Ray Photon Correlation Spectroscopy in a Reflection Geometry: Coherence and Resolution. *Opt. Commun.* **2005**, *247*, 111–124.

(29) Gutt, C.; Ghaderi, T.; Tolan, M.; Sinha, S. K.; Gruebel, G. Effects of Partial Coherence on Correlation Functions Measured by X-Ray Photon Correlation Spectroscopy. *Phys. Rev. B* **2008**, *77*, 094133.

For Table of Contents Only: